



## A railway local degraded adhesion model including variable friction, energy dissipation and adhesion recovery

Martina Meacci , Zhiyong Shi , Elisa Butini , Lorenzo Marini , Enrico Meli & Andrea Rindi

To cite this article: Martina Meacci , Zhiyong Shi , Elisa Butini , Lorenzo Marini , Enrico Meli & Andrea Rindi (2020): A railway local degraded adhesion model including variable friction, energy dissipation and adhesion recovery, Vehicle System Dynamics, DOI: [10.1080/00423114.2020.1775266](https://doi.org/10.1080/00423114.2020.1775266)

To link to this article: <https://doi.org/10.1080/00423114.2020.1775266>



Published online: 10 Jun 2020.



Submit your article to this journal [↗](#)



Article views: 87




View related articles [↗](#)



View Crossmark data [↗](#)



# A railway local degraded adhesion model including variable friction, energy dissipation and adhesion recovery

Martina Meacci, Zhiyong Shi , Elisa Butini, Lorenzo Marini, Enrico Meli and Andrea Rindi

Department of Industrial Engineering, University of Florence, Florence, Italy

## ABSTRACT

The modelling of the wheel–rail contact is fundamental in the railway field since the contact forces directly affect vehicle dynamics, wear, safety and maintenance. In this context, the development of a realistic adhesion model able to describe degraded adhesion conditions is still an open problem because of the complex non-linear behaviour of the adhesion coefficient. To face this problem, in this work an innovative degraded adhesion model has been developed taking into account important phenomena like large sliding at the contact interface, the consequent energy dissipation and the adhesion recovery caused by the cleaning effect on the rail due to the friction forces. The new approach, based on FASTSIM algorithm and Polach theory, is numerically very efficient and has been specifically designed for multibody applications. The developed model has been validated through the comparison with experimental data related to suitable braking manoeuvres.

## ARTICLE HISTORY

Received 20 November 2018  
Revised 20 January 2020  
Accepted 29 March 2020

## KEYWORDS

Adhesion; wheel–rail contact; multibody modelling; railway vehicles

## 1. Introduction

The accurate modelling of the wheel–rail contact is a fundamental task in the railway field since the contact forces are strongly connected with vehicle dynamics, safety, wear and maintenance. Typically, simplified and efficient multibody contact models consist of three main tasks: the contact point calculation, the normal problem solution and the tangential problem solution, including the adhesion model. The contact point detection allows the calculation of the contact point position on the wheel and rail surfaces. The main approaches in the literature make use of constraint formulations [1] or analytical procedures focused on the algebraic problem dimension reduction [2–4]. Typically, the normal problem is solved by using Lagrange multipliers [5,6] or Hertz theory [7–9]. As regards the tangential problem, many approaches have been taken into account in the last years. The most famous strategies comprise the linear Kalker theory (saturated according to Johnson-Vermulen formula [10–13]), the non-linear Kalker theory implemented in the FASTSIM algorithm [13–16], and Polach theory [17,18] that considers variable adhesion coefficient (decreasing with increasing creepages) in absence of contact spin.

The tangential problem is particularly challenging because, due to the complex non-linear behaviour of the adhesion coefficient and the presence of external unknown contaminants (third body layer), the development of a realistic adhesion law turns out to be quite hard. This is especially true when degraded adhesion and the large sliding at the wheel–rail interface yield a high energy dissipation and, consequently, an adhesion recovery. The adhesion recovery is generated by the cleaning effect of the sliding that removes the debris at the contact surface and it becomes quite significant under degraded adhesion conditions. In fact, the final adhesion recovery caused by the removal of external contaminants may deeply affect both the vehicle dynamics and the traction and braking manoeuvres. The cleaning effect has been taken into account in previous studies as additional flexibility [7,13] and varying parameters [1,17], or by the introduction of transient adhesion characteristics [19]. During the years, many studies have been performed to investigate the role of the third body between the contact surfaces and many analyses have been carried out through both laboratory test rigs and on-track railway tests [20–27]. At the same time, specific phenomena like the dissipation of energy and the adhesion recovery have begun to be more accurately studied to have a better understanding of the non-linear behaviour of the degraded adhesion [28–30].

In some previous preliminary papers [31–34], the authors have focused on ‘global’ degraded adhesion models (i.e. models involving global sliding / creepages and forces) and have extended the Polach theory [1,17,18] to take into account the degraded adhesion effects. In this work, the authors present a new ‘local’ degraded adhesion model directly connecting local sliding / creepages inside the contact area to the local contact pressures. The effects of the energy dissipation due to the large sliding occurring at the contact interface, of the consequent cleaning action on the rail caused by the large sliding and of the resulting adhesion recovery due to the removal of the external contaminant have been carefully taken into account by properly extending the FASTSIM algorithm [7,13]. To reach this goal, the friction coefficient has been considered variable inside the contact area. In this way, the adhesion recovery phenomenon can be investigated much more in detail with respect to global approaches. A previous step towards this direction (i.e. considering a variable friction coefficient inside local adhesion models) can be found in [35,36] where the authors proposed a first preliminary and approximated approach to face the problem.

The presented model can be applied to all the main scenarios in the railway field, i.e. presence of multiple contact points, different wheel and rail profiles, generic railway tracks, etc. Furthermore, as railway dynamic simulations are usually carried out by means of multi-body models, the new adhesion model has to be implemented directly online and in ‘real time’ within the multibody codes (e.g. Matlab-Simulink or Simpack environments) and, consequently, has to guarantee a good trade-off between accuracy and numerical efficiency. For this reason, since the numerical performance is a primary concern, it is impossible in practise to model the contact by considering the wheel and the rail as generic elastic continuous bodies [15].

Finally, the adhesion model has been preliminarily validated through experimental data coming from specific railway braking tests under degraded adhesion conditions performed by Trenitalia S.p.a. in Velim (Czech Republic) on a straight track with the coach UIC-Z1 [37,38]. The preliminary results are encouraging: the model has shown a good accuracy in reproducing the complex nonlinear behaviour of the system and, at the same time, good numerical efficiency.

In Section 2 the general architecture of the model is explained. In Section 3 the modelling details are described, paying attention to the tangential problem. Sections 4 and 5 introduce the experimental data and the validation of the new model. Further simulation results are presented in Section 6 and conclusions and future developments are proposed in Section 7.

## 2. General architecture of the model

The multibody model is composed of two main parts interacting during the simulation: the 3D railway vehicle model and the 3D wheel–rail contact model (Figure 1; see [33,35,36] as well).

At each numerical step of the simulation, the multibody vehicle model computes the kinematic wheel quantities (position  $\underline{G}_w$ , orientation  $\underline{\Phi}_w$ , velocity  $\underline{v}_w$  and angular velocity  $\underline{\omega}_w$ ) and the contact model, using such variables as inputs, calculates the normal and tangential contact pressures  $p_n, p_t$  applied to the wheel into the contact area associated to the contact point  $\underline{P}_c$ , the sliding  $s$  in the contact patch and the friction coefficient  $\mu$  inside the contact area.

Typically, simplified and efficient multibody contact models are characterised by three main submodels: the contact point ( $\underline{P}_c$ ) detection [4,16,39], the normal problem, solved by using the global Hertz theory to calculate the normal contact pressures ( $p_n$ ), and the tangential problem to compute the tangential contact pressures  $p_t$ , the sliding  $s$  and the friction coefficient  $\mu$  (Figure 2 [33,35,36]). The tangential problem solution relies on the local degraded adhesion model described by the authors in this work. The inputs of the degraded adhesion model are the wheel kinematic variables, the position  $\underline{G}_w$ , the orientation  $\underline{\Phi}_w$ , the wheel velocity  $\underline{v}_w$ , the wheel angular velocity  $\underline{\omega}_w$ , the normal pressures at the contact interface  $p_n$  and the position of the contact points  $\underline{P}_c$ . The local degraded adhesion contact model enables the calculation of tangential pressures  $p_t$ , sliding  $s$  and friction coefficient inside the discretised contact patch by extending the Kalker's FASTSIM algorithm to properly take into account energy dissipation and adhesion recovery.

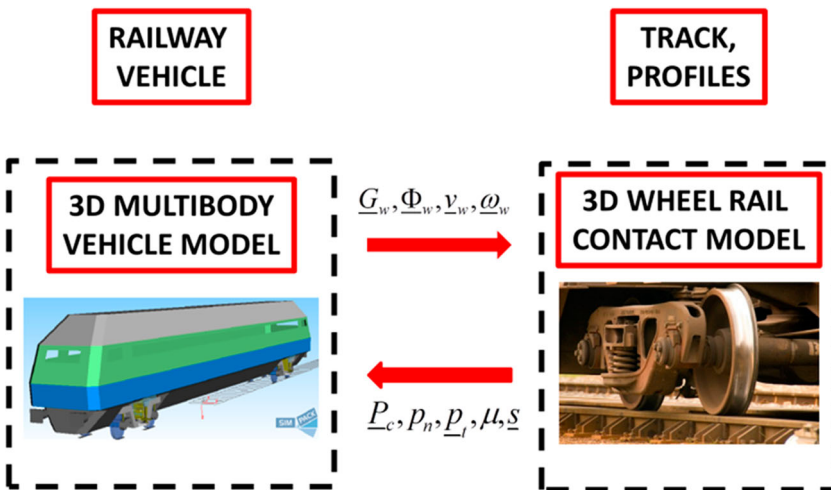


**Figure 1.** Architecture of the multibody model [33,35,36].

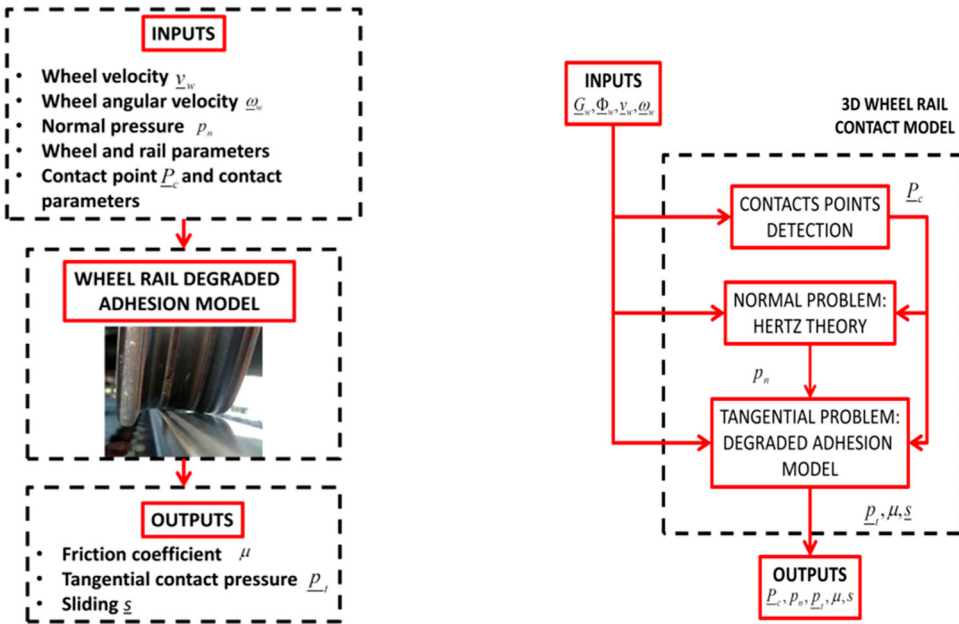


**Figure 2.** Inputs and outputs of the degraded adhesion model and architecture of the wheel–rail contact model [33,35,36].

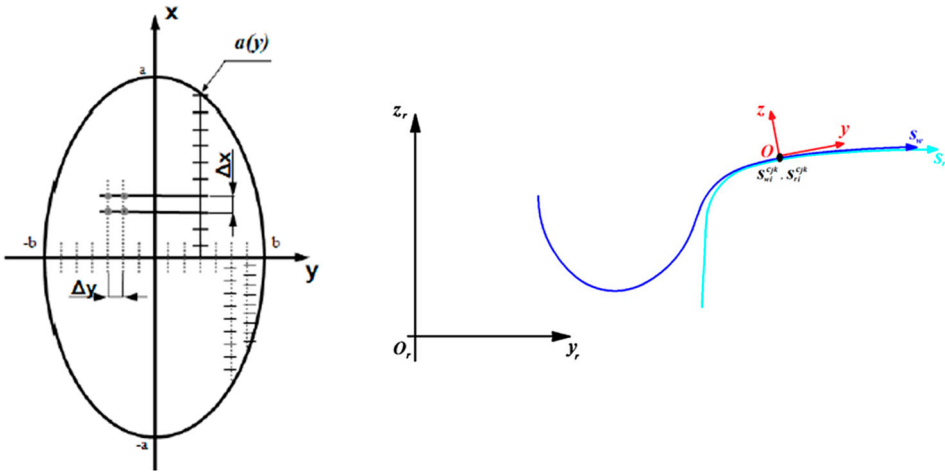
### 3. Modelling

This chapter consists of three subsections presenting the detailed description of the new degraded adhesion problem, the wheel–rail contact model and the multibody vehicle model, respectively.

#### 3.1. Local adhesion model

The new degraded adhesion model, on which the tangential contact model is based, is an improvement of the Polach adhesion law [1,17] and of the FASTSIM algorithm [7,13]. Unlike what the authors have done in previous works on this topic [31–34], in this work, the new adhesion model is ‘local’ and directly connects the local sliding / creepages inside the contact area to the local pressures. The effects of the energy dissipation due to the large sliding occurring at the contact interface, of the consequent large sliding cleaning action on the rail and of the resulting adhesion recovery caused by the removal of the external contaminant have been carefully taken into account by developing a new local friction law to be used inside the extended version of the FASTSIM algorithm. To reach this goal, the friction coefficient has been considered variable inside the contact area and function of the local sliding and dissipated energy. A first preliminary and approximated approach to face this problem (i.e. considering a variable friction coefficient inside local adhesion models) can be found in [35,36].

To calculate the local tangential contact variables (tangential contact pressures  $p_t$  and local sliding  $s$  within the contact patch), the corresponding normal pressures  $p_n$ , the



(a). Contact patch discretization (b). Normal abscissa for the wheel and rail profile.

**Figure 3.** The reference system at the wheel–rail interface [35,36]. (a) Contact patch discretisation. (b) Normal abscissa for the wheel and rail profile.

contact points position  $\underline{P}_{cW}$  and the wheel kinematic variables  $\underline{G}_w$ ,  $\underline{v}_w$ ,  $R$  and  $\underline{\omega}_w$  (position, orientation and their derivatives) are supposed to be known (see Figures 1 and 2).

A new reference system is defined at the wheel–rail interface on the contact plane (i.e. the common tangent plane between the wheel and rail surfaces): the  $x$  and  $y$  axes are the longitudinal and the transversal direction of the contact plane, respectively, while  $z$  is the normal axis, (see Figure 3).

The first step consists in the discretisation of the contact surface: from Hertz theory, the elliptical contact patch and its semi-axes  $a$  and  $b$  are discretised in a bidimensional grid (by using a not constant grid resolution) where the quantities  $p_n$ ,  $p_t$  and  $\underline{s}$  will be evaluated.

Initially, the transversal axis (with respect to the motion direction) of the contact ellipse has been divided in  $(n_y - 1)$  equal parts of magnitude  $\Delta y$  by means of  $n_y$  equidistant nodes. Then the longitudinal sections of the patch have been divided in  $(n_x - 1)$  equal parts of magnitude  $\Delta x$  by means of  $n_x$  equidistant nodes, as shown in Figure 3(a):

$$\Delta y = \frac{2b}{n_y - 1}, \quad \Delta x(y) = \frac{2a(y)}{n_x - 1} \quad a(y) = a\sqrt{1 - \frac{y^2}{b^2}} \quad (1)$$

Thanks to this strategy, the longitudinal grid resolution is not constant but increases near the lateral edges of the ellipse, where the lengths  $a(y)$  are smaller. This procedure provides more accurate results right next to the edges of the ellipse, where a constant resolution grid would generate excessive numerical noise. The values of the  $n_x$  and  $n_y$  parameters have to assure the right balance between accuracy and computational load; good values of compromise are in the range 25–50.

The extended version of the FASTSIM algorithm is always based on the proportionality hypothesis between the tangential contact pressure  $\underline{p}_t$  and the tangential elastic displacements  $\underline{u}_t$ , both evaluated within the contact patch [6,14,16]:

$$\underline{u}_t(x, y) = L\underline{p}_t(x, y) \quad L = L(\underline{\varepsilon}, a, b, G, \nu) \quad (2)$$

where the flexibility  $L$  (function of the global rigid creepages  $\underline{\varepsilon}$ , the semi axes of the contact patch  $a$ ,  $b$ , the wheel and rail combined shear modulus  $G$  and the wheel and rail combined Poisson's ratio  $\nu$ ) can be calculated as follows:

$$L = \frac{|\varepsilon_x|L_1 + |\varepsilon_y|L_2 + c|\varepsilon_{sp}|L_3}{(\varepsilon_x^2 + \varepsilon_y^2 + c^2\varepsilon_{sp}^2)^{1/2}}$$

$$\underline{v}_{pc} = \underline{v}_\omega + \omega_w \times (\underline{P}_c - \underline{G}_w)$$

$$\varepsilon_x = v_{pcx}/\|\underline{v}_w\|$$

$$\varepsilon_y = v_{pcy}/\|\underline{v}_w\|$$

$$\varepsilon_{sp} = \frac{\omega_w \cdot \underline{n}}{\|\underline{v}_w\|} \quad (3)$$

with  $L_1 = 8a/(3GC_{11})$ ,  $L_2 = 8a/(3GC_{22})$ ,  $L_3 = \pi a^2/(4GC_{23})$  and  $c = \sqrt{ab}$  (the constants  $C_{ij}$ , functions both of the Poisson's ratio  $\nu$  and of the ratio  $a/b$ , are the Kalker's parameters and can be found in the literature [7]). The local sliding  $\underline{s}$  can be calculated by derivation considering both the elastic creepages and the rigid ones:

$$\underline{s}(x, y) = \dot{\underline{u}}_t(x, y) + V \begin{pmatrix} e_x \\ e_y \end{pmatrix} \quad (4)$$

with

$$\begin{pmatrix} e_x \\ e_y \end{pmatrix} = \begin{pmatrix} \varepsilon_x - y_j \varepsilon_{sp} \\ \varepsilon_y - x_i \varepsilon_{sp} \end{pmatrix} \quad (5)$$

where  $V = \|\underline{v}_\omega\|$  is the longitudinal vehicle speed,  $e_x$ ,  $e_y$  are the local rigid creepages and  $\varepsilon_x$ ,  $\varepsilon_y$ ,  $\varepsilon_{sp}$  are the global rigid creepages. Once the contact patch is discretised, the FASTSIM algorithm allows the iterative evaluation of both the contact pressures  $p_n$ ,  $\underline{p}_t$  and the local sliding  $\underline{s}$  in order to divide the contact patch into adhesion and slip zone. Indicating the generic point of the grid with  $(x_i, y_j)$ ,  $1 \leq i \leq n_x$ ,  $1 \leq j \leq n_y$ , the normal contact pressure can be expressed as:

$$p_n(x_i, y_j) = \frac{3}{2} \frac{N_c}{\pi ab} \sqrt{1 - \frac{x_i^2}{a^2} - \frac{y_j^2}{b^2}} \quad (6)$$

where  $N_c$  is the normal contact force, while the limit adhesion pressure  $\underline{p}_A$  is:

$$\underline{p}_A(x_i, y_i) = \underline{p}_t(x_{i-1}, y_j) - \begin{pmatrix} e_x \\ e_y \end{pmatrix} \frac{\Delta x(y_i)}{L} \quad (7)$$

Thus, knowing the variable values in the point  $(x_{i-1}, y_j)$ , it is possible to go to the point  $(x_i, y_j)$  as follows:

if  $\|\underline{p}_A(x_i, y_j)\| \leq \mu(x_i, y_j)p_n(x_i, y_j)$

$$\begin{cases} \underline{p}_t(x_i, y_j) = \underline{p}_A(x_i, y_j) \\ \underline{s}(x_i, y_j) = 0 \end{cases} \quad (8)$$

if  $\|\underline{p}_A(x_i, y_j)\| > \mu(x_i, y_j)p_n(x_i, y_j)$

$$\begin{cases} \underline{p}_t(x_i, y_j) = \mu(x_i, y_j)\underline{p}_n(x_i, y_j)\underline{p}_A(x_i, y_j)/\|\underline{p}_A(x_i, y_j)\| \\ \underline{s}(x_i, y_j) = \frac{LV}{\Delta x(y_j)}[\underline{p}_t(x_i, y_j) - \underline{p}_A(x_i, y_j)] \end{cases} \quad (9)$$

where  $\mu(x_i, y_i)$  is the friction coefficient in  $(x_i, y_i)$ ; Equations (8) and (9) hold in the adhesion and slip zone, respectively. Iterating the procedure for  $2 \leq i \leq n_x$  and successively for  $1 \leq j \leq n_y$ , and assuming as boundary conditions  $\underline{p}_t(x_1, y_j) = 0$ ,  $\underline{s}(x_1, y_j) = 0$  for  $1 \leq j \leq n_y$  (i.e. stresses and sliding zero out of the contact patch), the desired distribution of  $p_n(x_i, y_j)$ ,  $\underline{p}_t(x_i, y_j)$  and  $\underline{s}(x_i, y_j)$  can be determined.

In the previous equations, the local value of the friction coefficient  $\mu(x_i, y_j)$  is still unknown, and has to be modelled. The main phenomena characterising the degraded adhesion are the large sliding occurring at the contact interface and, consequently, the high energy dissipation. Such a dissipation causes a cleaning effect on the contact surfaces and, finally, an adhesion recovery due to the removal of external contaminants. When the specific dissipated energy  $W_{sp}$  is low, the cleaning effect is almost absent, the contaminant level  $h$  does not change and the friction coefficient  $\mu$  is equal to its original value in degraded adhesion conditions  $\mu_d$ . As the energy  $W_{sp}$  increases, the cleaning effect increases too, the contaminant level  $h$  becomes thinner and the adhesion coefficient  $\mu$  raises. In the end, for large values of  $W_{sp}$ , all the contaminant is removed ( $h$  is null) and the adhesion coefficient  $\mu$  reaches its maximum value  $\mu_r$ ; the adhesion recovery due to the removal of external contaminants is now completed. At the same time, if the energy dissipation begins to decrease, due for example to a lower sliding, the reverse process occurs. Figure 4 illustrates the friction coefficient  $\mu$  as a function of the sliding  $s$  in a standard situation and in presence of dissipated energy  $W_{sp}$  at the contact interface.

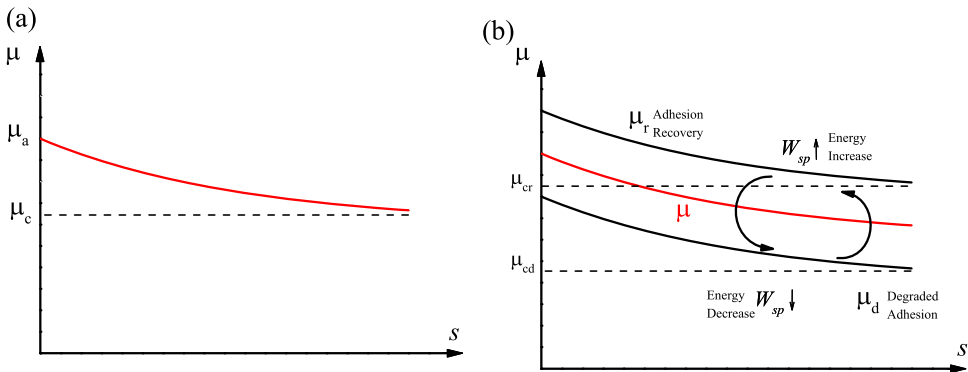


**Figure 4.** Friction coefficient  $\mu$  as function of the sliding  $s$ : (a) standard behaviour (b) behaviour in presence of dissipated energy  $W_{sp}$  at the contact interface [35,36].



Since the contaminant level and its characteristics are usually unknown, it is useful trying to experimentally correlate the friction coefficient  $\mu$  directly with the specific dissipated energy  $W_{sp}$ . To reproduce the qualitative trend previously described and to allow the friction coefficient to vary between the extreme values  $\mu_d$  and  $\mu_r$ , the following expression for  $\mu$  is proposed:

$$\mu = [1 - \lambda(W_{sp})]\mu_d + \lambda(W_{sp})\mu_r \quad (10)$$

where  $\lambda(W_{sp})$  is an unknown transition function between degraded adhesion and adhesion recovery. The function  $\lambda(W_{sp})$  has to be positive and monotonous increasing; moreover, the following boundary conditions are supposed to be verified:  $\lambda(0) = 0$  and  $\lambda(+\infty) = 1$ . This way it is supposed that the transition between degraded adhesion and adhesion recovery only depends on  $W_{sp}$ . This hypothesis is obviously only an approximation but, as it will be clearer in the next chapters, it well describes the adhesion behaviour.

Initially, to catch the physical essence of the problem without introducing a large number of unmanageable and unmeasurable parameters, a simple expression for  $\lambda(W_{sp})$  is assumed:

$$\lambda(W_{sp}) = 1 - e^{-\tau|W_{sp}|} \quad (11)$$

where  $\tau$  is now the only unknown parameter to be tuned on the base of the experimental data. In this research activity, the two main friction coefficients  $\mu_d$  and  $\mu_r$  (degraded adhesion and adhesion recovery) have been calculated according to:

$$\begin{cases} \mu_d(x_i, y_j) = \left( \frac{\mu_{cd}}{A_d} - \mu_{cd} \right) e^{-s(x_i, y_j)\gamma_d} + \mu_{cd} \\ \mu_r(x_i, y_j) = \left( \frac{\mu_{cr}}{A_r} - \mu_{cr} \right) e^{-s(x_i, y_j)\gamma_r} + \mu_{cr} \end{cases} \quad (12)$$

where  $s = \|\underline{s}\|$ ,  $\mu_{cd}$ ,  $\mu_{cr}$  are the kinematic values of  $\mu_d$ ,  $\mu_r$ ,  $A_d$ ,  $A_r$  are the ratios between the kinetic friction coefficients and the static ones, and  $\gamma_r$ ,  $\gamma_d$  are the parameters that describe the friction decay as the sliding increases. Consequently, according to the previous consideration,  $\mu$  can be written as:

$$\begin{cases} \mu(x_i, y_j) = (1 - \lambda)\mu_d(x_i, y_j) + \lambda\mu_r(x_i, y_j) \\ \lambda = 1 - e^{-\tau|W_{sp}|} \end{cases} \quad (13)$$

The specific dissipated energy  $W_{sp}$  can be evaluated as:

$$W_{sp}(x_i, y_j) = \underline{p}_t(x_i, y_j) \cdot \underline{s}(x_i, y_j) \quad (14)$$

At this point, the calculation of the unknowns  $\underline{p}_t(x_i, y_j)$  and  $\underline{s}(x_i, y_j)$  is not so simple because Equations (8, 9, 12–14) constitute a system of non-linear equations to be solved numerically. To this aim, it can be observed that, thanks to Equations (8) and (9), the quantities  $\underline{p}_t(x_i, y_j)$  and  $\underline{s}(x_i, y_j)$  can be written as a function of  $\mu(x_i, y_j)$ :

$$\begin{cases} \underline{p}_t(x_i, y_j) = \underline{p}_t(\mu(x_i, y_j)) \\ \underline{s}(x_i, y_j) = \underline{s}(\mu(x_i, y_j)) \end{cases} \quad (15)$$

Consequently, the specific dissipated energy  $W_{sp}(x_i, y_j) = W_{sp}(\mu(x_i, y_j))$ , the degraded and recovered friction coefficients  $\mu_d(x_i, y_j) = \mu_d(\mu(x_i, y_j))$ ,  $\mu_r(x_i, y_j) = \mu_r(\mu(x_i, y_j))$

and the transition function  $\lambda(x_i, y_j) = \lambda(\mu(x_i, y_j))$  are functions of  $\mu(x_i, y_j)$  as well. Inserting such relations into equation (13), one finally gets the following non-linear scalar equation in the unknown  $\mu(x_i, y_j)$ :

$$\mu(x_i, y_j) = F(\mu(x_i, y_j)) \quad (16)$$

where  $F$  indicates the generic functional dependence. Due to the simplicity of the transition function  $\lambda(W_{sp})$ , the numerical solution of (16) can be easily obtained through standard non-linear solvers [40]. Eventually, once  $\mu(x_i, y_j)$  is known,  $\underline{p}_t(x_i, y_j)$  and  $\underline{s}(x_i, y_j)$  can be immediately evaluated in the point  $(x_i, y_j)$  of the grid by means of Equations (8) and (9).

This process is repeated for each point of the grid that discretises the contact patch and requires boundary conditions on the points  $(x_1, y_j)$ . In particular, sliding  $\underline{s}$  and pressures  $\underline{p}_t$  on the edge of the contact patch are set equal to zero, while the adhesion coefficients  $\mu_d$ ,  $\mu_r$  are taken equal to the static values:

$$\begin{cases} \underline{s}(x_1, y_j) = \underline{0} \\ \underline{p}_t(x_1, y_j) = \underline{0} \\ \begin{cases} \mu_d(x_1, y_j) = \mu_{cd}/A_d \\ \mu_r(x_1, y_j) = \mu_{cr}/A_r \end{cases} \\ \mu(x_1, y_j) = \mu_d(x_1, y_j) \\ \text{with } W_{sp}(x_1, y_j) = 0 \end{cases} \quad (17)$$

Finally, it is possible to evaluate the tangential force acting on the contact patch area by integration:

$$\begin{aligned} \underline{T}_x &= \int \underline{p}_{tx} dA \\ \underline{T}_y &= \int \underline{p}_{ty} dA \\ \underline{M}_{sp} &= \int_A (xp_{ty} - yp_{tx}) dA \\ \underline{T}_c &= \underline{T}_x J_1 + \underline{T}_y J_2 \\ \underline{M}_{sp} &= \underline{M}_{sp} \underline{n} \end{aligned} \quad (18)$$

### 3.2. Wheel-rail contact model

As introduced in Section 2, the wheel-rail contact model inputs are the kinematic variables of each wheel (position  $\underline{G}_w$ , orientation  $\underline{\Phi}_w$ , velocity  $\underline{v}_w$  and angular velocity  $\underline{\omega}_w$ ) together with the track geometry and the wheel and rail profiles. The outputs are the normal and tangential contact pressures  $p_n$ ,  $\underline{p}_t$  (applied to the wheel in correspondence of the contact point  $\underline{P}_c$ ), the sliding  $\underline{s}$  and the friction coefficient  $\mu$ . The details concerning the contact points detection algorithms and the normal contact models used in this work can be found in [4,16,32,33,39].

### 3.3. Multibody vehicle model

The multibody vehicle model has been developed to investigate the dynamic behaviour of the vehicle, an UIC-Z1 wagon operated by Trenitalia S.p.a [37] (see Figure 5).

The vehicle consists of one carbody, two bogie frames, eight axle boxes and four wheelsets. The primary suspension comprises flex coil springs, vertical hydraulic dampers



**Figure 5.** The UIC-Z1 vehicle.

and axle box bushings, and links the bogie frame to the four axle boxes. At the same time, the secondary suspension comprises vertical, lateral and longitudinal ant-yaw dampers, lateral bump-stops, anti-roll bar and traction rod, and links the carbody to the bogie frames.

The multibody vehicle model describes the main degrees of freedom (DOFs) of the system bodies (one carbody, two bogie frames, eight axle boxes, and four wheelsets). The total number of DOFs is equal to 50.

The standard wheel and rail profiles ORE S 1002 and UIC 60 have been considered. The main parameters of the railway vehicle are reported in Table 1 while most important inertial parameters are listed in Table 2. The primary (comprising springs, dampers and axle box bushings) and the secondary (comprising springs, dampers, lateral bump-stops, anti-roll bar and traction rod) suspension stages have been described by means of 3D linear and non-linear visco-elastic force elements.

Table 3 summarises the characteristics of the main linear elastic force elements of both the suspension. Eventually, the UICZ1 Wheel Slide Protection (WSP) system has been described as well to correctly reproduce the vehicle dynamics during the braking manoeuvres under degraded adhesion conditions [38].

**Table 1.** Main geometric characteristics of the railway vehicle layout.

Parameters	Units	Value
Total mass	(kg)	43,000
Bogie wheelbase	(m)	2.56
Bogie distance	(m)	19
Wheel diameter	(m)	0.89

**Table 2.** Main inertial properties of the rigid bodies of the railway system.

Body	Mass (kg)	$I_{xx}$ (kgm <sup>2</sup> )	$I_{yy}$ (kgm <sup>2</sup> )	$I_{zz}$ (kgm <sup>2</sup> )
Carbody	≈ 29,000	76,400	1,494,400	1,467,160
Bogie	≈ 3000	2400	1900	4000
Wheelset	≈ 1300	800	160	800
Axlebox	≈ 200	3	12	12

**Table 3.** Linear elastic characteristics of the two stage suspensions of the railway vehicle.

Element		Primary suspension	Secondary suspension	Axle bushing	Anti-roll bar
Transl. Stiff. x	(N/m)	844,000	124,000	40,000,000	0
Transl. Stiff. y	(N/m)	844,000	124,000	6,500,000	0
Transl. Stiff. z	(N/m)	790,000	340,000	40,000,000	0
Rotat. Stiff. x	(Nm/rad)	10,700	0	45,000	2,500,000
Rotat. Stiff. y	(Nm/rad)	10,700	0	9700	0
Rotat. Stiff. z	(Nm/rad)	0	0	45,000	0

#### 4. Experimental campaign and measured data

Usually, to validate this kind of adhesion model, braking tests are quite useful due to the critical operating conditions which characterise braking manoeuvres (large sliding, high energy dissipation, possible presence of degraded adhesion, etc.). Unfortunately, a direct experimental validation of such models in terms of contact pressures (at a local level) is almost impossible on-field (it is very difficult in laboratory too). Therefore, in such circumstances, a good compromise to get a preliminary validation of the adhesion models is to compare experimental and simulated results in terms of velocities, forces and global sliding (that is at a global level).

The local degraded adhesion model has been validated by means of experimental data provided by Trenitalia s.p.a. and coming from on-track tests performed in Velim (Czech Republic) with the coach UIC-Z1 ([37,38]). The considered vehicle is equipped with a fully-working WSP system. The experimental tests have been carried out on a straight railway track. The wheel profile is the ORE S1002 (with a wheelset width  $d_w$  equal to 1.5 m and a wheel radius  $r$  equal to 0.445 m) while the rail profile is the UIC60 (with a gauge  $d_r$  equal to 1.435 m and a laying angle equal to  $1/20$  rad).

In Table 4 the main wheel, rail and contact parameters are reported. The kinetic friction coefficient under degraded adhesion conditions  $\mu_{cd}$  changes depending on the specific test (see [31,33,34]). On the contrary, the kinetic friction coefficient under full adhesion recovery  $\mu_{cr}$  depends on the wheel and rail material and represents the kinetic friction coefficient under dry conditions.

In the considered campaign, for each experimental test, the following physical variables have been measured (acquisition time  $\Delta t_s$  equal to 0.01s):

- the longitudinal vehicle velocity  $v_v^{sp}$  (the longitudinal wheel velocities  $v_{wj}^{sp}$  ( $j$  represents the  $j$ -th wheel) are taken equal to  $v_v^{sp}$ ).

**Table 4.** Wheel–rail contact parameters used in the contact model.

Parameters	Unit	Value
Young modulus	(Pa)	$2.1 \cdot 10^{11}$
Shear modulus	(Pa)	$8 \cdot 10^{10}$
Poisson coefficient	(–)	0.3
Kinetic friction coefficient $\mu_{cd}$	–	0.06
Kinetic friction coefficient $\mu_{cr}$	–	0.28
Friction ratio $A_d$	–	0.4
Friction ratio $A_r$	–	0.4
Friction decrease rate $\gamma_d$	(s/m)	0.2
Friction decrease rate $\gamma_r$	(s/m)	0.6

- the wheels angular velocities  $\omega_{wj}^{sp}$ . The angular accelerations  $\dot{\omega}_{wj}^{sp}$  are evaluated by derivation and by filtering the signals.
- the vertical forces  $N_{wj}^{sp}$  on the vehicle wheels. In practice, the vertical forces on the wheels  $N_{wj}^{sp}$  are approximately calculated by measuring the primary suspension deflections. Finally, the vertical contact forces  $N_{cj}^{sp}$  have been approximately computed starting from  $N_{wj}^{sp}$  and by subtracting the wheel weight. This procedure is for sure approximated and the vertical force dynamic components are considered only in an approximated way. However, it represents a good compromise between measurement accuracy and cost / duration / complexity of the experimental campaign.
- the braking torques  $C_{wj}^{sp}$  applied to the wheels. The braking torques applied to the wheels have been estimated starting from the measurements of the braking pressures provided by the vehicle owner and from the knowledge of the braking plant characteristics. In this specific case study, the geometry and the physical features of the braking plant components were known for the considered vehicle. At the same time, both the geometry of wheelsets and braking disks and their physical features were known as well. Naturally, some uncertainties are present as, for example, on the braking disk friction value and on its behaviour as a function of the temperature. As in the previous case, the measurement procedure is approximated but represents again a good compromise

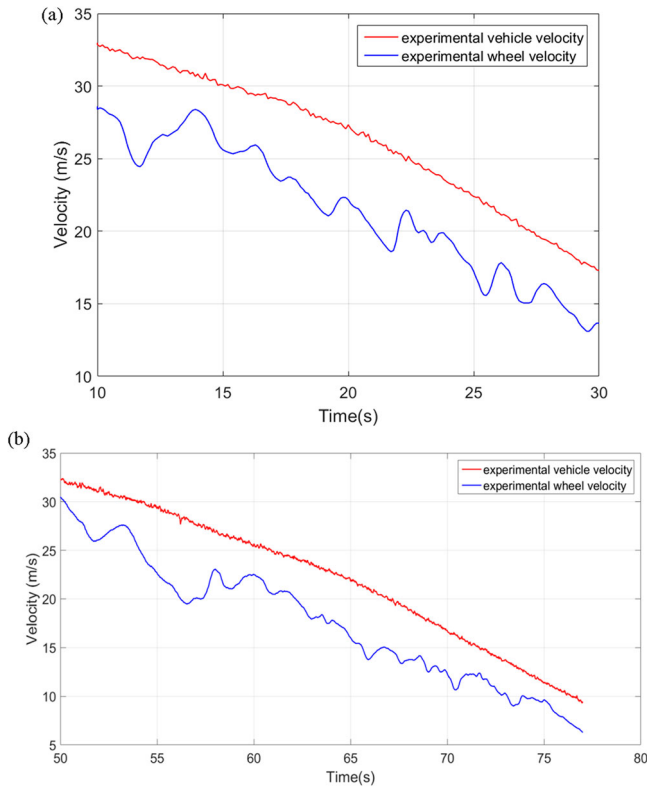


**Figure 6.** Experimental trend of the vehicle velocity  $v_{w1}^{sp}$  and wheel velocity  $r\omega_{w1}^{sp}$  (first wheelset) for two braking manoeuvres: (a) test A; (b) test B.

between measurement accuracy and cost / duration / complexity of the experimental campaign.

For instance, in Figure 6 the wheel longitudinal and rotational velocities  $v_{w1}^{sp}$  and  $r\omega_{w1}^{sp}$  (first wheelset) are plotted for two of the tests performed during the experimental campaign (named test A and test B); the WSP intervention and the adhesion recovery during the second part of the braking manoeuvre can be easily observed.

The chosen tests start from a vehicle velocity of 32, 5m/s and, after few seconds, a braking torque is applied to each wheelset. The values of each braking torque are modulated by the WSP during the run of the train depending on the dynamics of the system.

## 5. Preliminary experimental validation of the local adhesion model

In this section, the model described in Section 3 is validated and the influence of the parameter  $\tau$  on the vehicle dynamics is analysed. More in detail, in chapter 5.1 the tuning of the model by using a specific set of experimental tests (namely, the test A) is described and the optimal value of the  $\tau$  parameter for this application is found. Subsequently, in chapter 5.2 the validation of the model by exploiting a different set of experimental tests (namely, the test B) is reported. In this case, both for the tuning and for the validation, suitable braking manoeuvres under degraded adhesion conditions have been considered.

### 5.1. Influence of the parameter $\tau$ on the vehicle dynamics and model tuning

In this preliminary phase, the effect of the parameter  $\tau$  on the dynamic response of the vehicle is investigated. Furthermore, the model is tuned by using a specific braking manoeuvre under degraded adhesion conditions (test A) and the optimal value of the  $\tau$  parameter for this application is found.

First of all, the behaviour of the system in absence of adhesion recovery ( $\tau = 0 \frac{m^2}{W}$ ) has been studied (see Figure 7). In this case the tangential contact problem is solved by means of the standard FASTSIM algorithm. As visible in Figure 7, despite the high sliding present during the braking manoeuvre and the consequent energy dissipation and cleaning effect on the rail, no adhesion recovery is observed (for example the slope of the vehicle velocity curve is quite constant). This effect is mainly due to the fact that the friction coefficient  $\mu$  is constant inside the contact area in the standard FASTSIM algorithm.

In Figure 8, the trend of the simulated first wheelset velocity  $r\omega_{w1}^{sp}$  is shown by varying only the parameter  $\tau$ . As it can be noticed, the adhesion increases as the parameter  $\tau$  grows until the limit condition  $\tau = 3 \cdot 10^{-8} \frac{m^2}{W}$ , corresponding to a completely recovered adhesion.

After this tuning phase, the optimised value chosen for  $\tau$  has been  $\tau = 8.1 \cdot 10^{-9} \frac{m^2}{W}$ . The optimal value has been calculated by minimising the error between simulated and experimental quantities via standard numerical techniques [40].

### 5.2. Model validation

In this section, the model is validated against experimental data by using a different braking manoeuvre under degraded adhesion conditions (test B). In this way, the capability of the

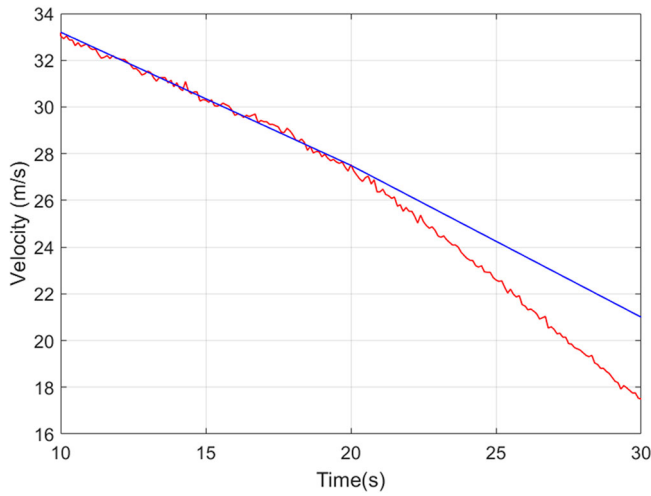


**Figure 7.** Experimental and simulated vehicle velocities  $v_{w1}^{sp}$ ,  $v_{w1}^{sm}$  in absence of adhesion recovery:  $\tau = 0m^2/W$  (obtained by using the standard FASTSIM).

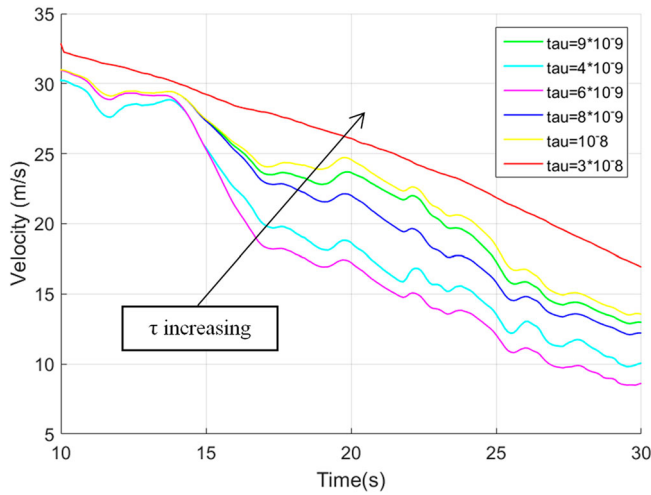


**Figure 8.** Simulated velocity of the first wheelset  $r\omega_{w1}^{sp}$  varying the parameter  $\tau$ .

model in approximating the complex and highly non-linear behaviour of the degraded adhesion is preliminarily evaluated.

The adhesion model validation is mainly focused on the velocities  $v_v^{sm}$ ,  $r\omega_{wj}^{sm}$ :  $v_v^{sm}$  is the longitudinal vehicle velocity,  $\omega_{wj}^{sm}$  is the rotational wheelset velocity and, for the sake of simplicity,  $r$  is always the nominal wheel radius. The simulated variables coming from the 3D multibody model  $v_v^{sm}$ ,  $r\omega_{wj}^{sm}$  have been compared with the correspondent experimental quantities  $v_v^{sp}$ ,  $r\omega_{wj}^{sp}$ . By way of example, the time histories of the velocities  $v_v^{sm}$ ,  $v_v^{sp}$  and  $r\omega_{w1}^{sm}$ ,  $r\omega_{w1}^{sp}$ , are reported in Figure 9 with a chosen  $\tau = 8 * 10^{-9} m^2/W$ .

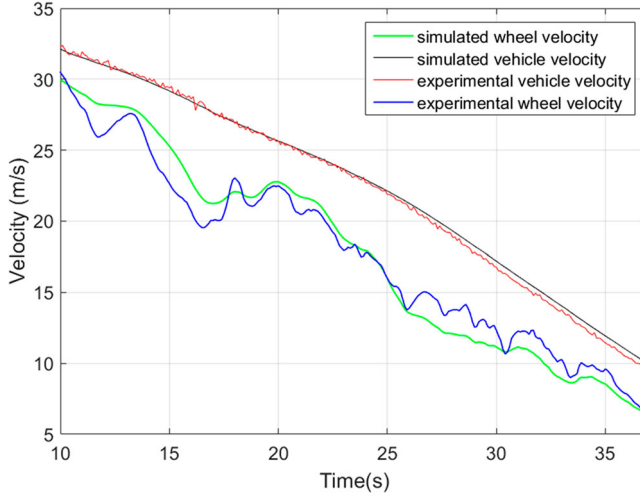


**Figure 9.** Comparison between the experimental and simulated longitudinal velocities of the vehicle  $v_V^{sm}, v_V^{sp}$  and the first wheelset  $r\omega_{w1}^{sm}, r\omega_{w1}^{sp}$ .

The showed results agrees quite well in terms of translational velocities  $v_V^{sm}, v_V^{sp}$ . As regards the velocities  $r\omega_{w1}^{sm}, r\omega_{w1}^{sp}$  the agreement is satisfying. However, these rotational velocities cannot be directly compared since the system is highly chaotic because of the presence of discontinuous and non-linear components as the WSP. To effectively compare the rotational velocities  $r\omega_{w1}^{sm}$  and  $r\omega_{w1}^{sp}$ , the statistical mean  $\bar{e}_j$  and standard deviations  $\Delta_j^e$  of the sliding estimation error  $e_j = s_j^{sm} - s_j^{sp}$  are exploited, in which simulated  $s_j^{sm}$  and experimental sliding  $s_j^{sp}$  are evaluated as:

$$s_j^{sm} = v_V^{sm} - r\omega_{wj}^{sm}, s_j^{sp} = v_V^{sp} - r\omega_{wj}^{sp} \quad (17)$$

As usual, the statistical indices are then determined as follows:

$$\bar{e}_j = \frac{1}{T_F - T_I} \int_{T_I}^{T_F} e_j dt, \Delta_j^e = \sqrt{\frac{1}{T_F - T_I} \int_{T_I}^{T_F} (e_j - \bar{e}_j)^2 dt} \quad (18)$$

where  $T_I$  and  $T_F$  are initial and final times of the simulation. By way of example, the mean  $\bar{e}_1$  and the standard deviation  $\Delta_1^e$  of the sliding estimation error  $e_1$  are reported in Table 5.

**Table 5.** Statistical comparison in terms of sliding estimation error and adhesion coefficient estimation error.

Parameters	Model	Mean $\bar{e}_1$	Standard deviation $\Delta_1^e$
Adhesion Coefficient (-): $f_1^{sm}, f_1^{sp}$	New 'local' adhesion model	0.0066	0.0044
Sliding (m/s): $s_1^{sm}, s_1^{sp}$	New 'local' adhesion model	1.21	0.75
Adhesion Coefficient (-): $f_1^{sm}, f_1^{sp}$	Previous 'global' adhesion model [32,33]	0.0089	0.0070
Sliding (m/s): $s_1^{sm}, s_1^{sp}$	Previous 'global' adhesion model [32,33]	1.50	0.90



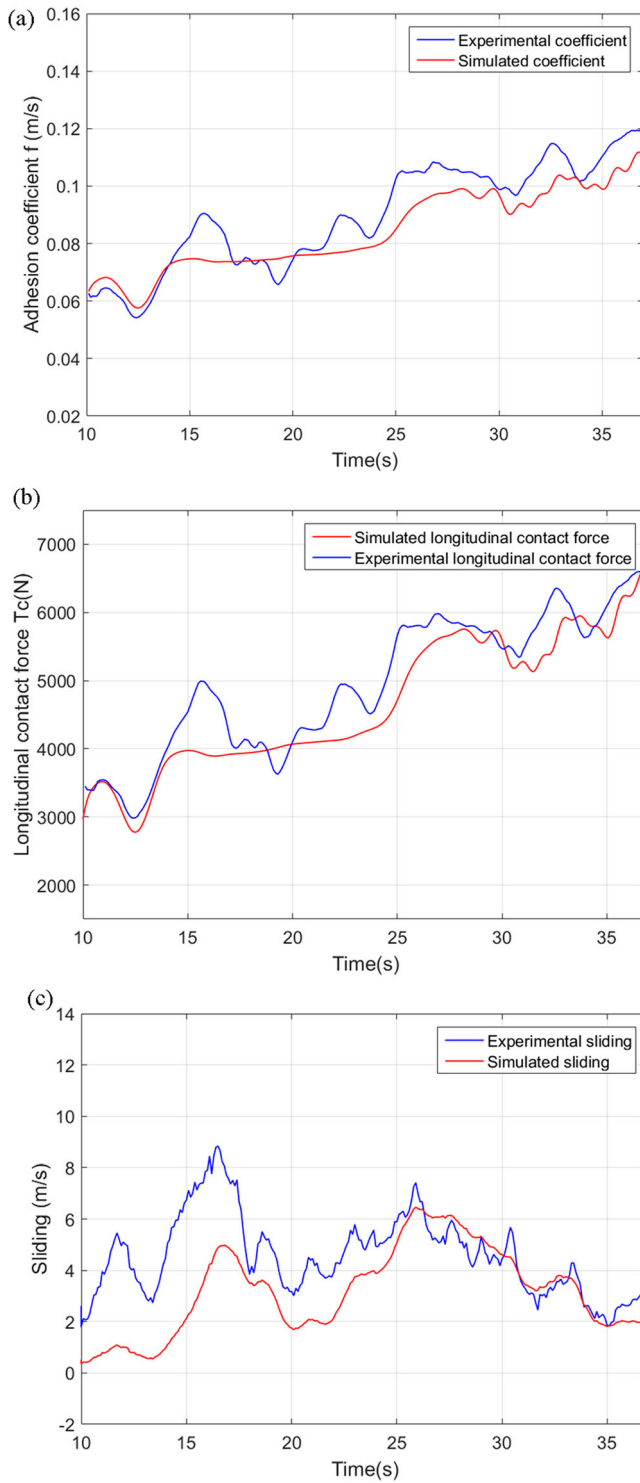


**Figure 10.** Comparison between experimental and simulated results for (a) adhesion coefficients  $f_1^{sp}$ ,  $f_1^{sm}$ , (b) longitudinal contact force  $T_{c1}^{sm}$ ,  $T_{c1}^{sp}$  and (c) sliding  $s_1^{sp}$ ,  $s_1^{sm}$ .

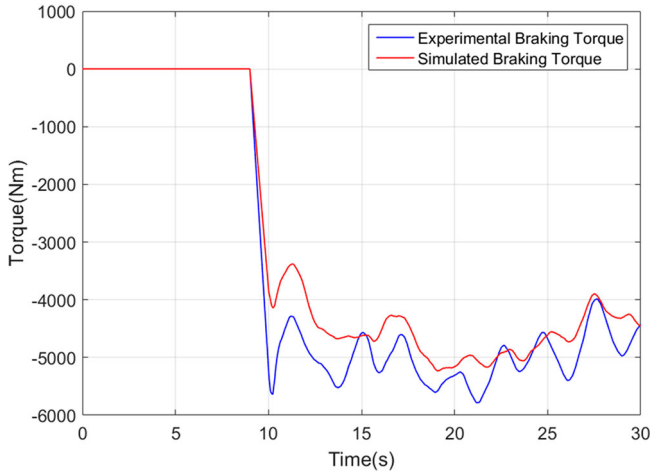


**Figure 11.** Comparison between experimental and simulated torques  $C_{w1}^{sp}$ ,  $C_{w1}^{sm}$  applied to the first wheelset of the vehicle.

In Figure 10(a) and in Table 5 (in terms of estimation error) the trend of the experimental and simulated adhesion coefficient  $f_j^{sp} = \frac{T_{cj}^{sp}}{N_j^{sp}}$ ,  $f_j^{sim} = \frac{T_{cj}^{sm}}{N_j^{sm}}$  is shown as well, where  $T_{cj}^{sp}$  and  $T_{cj}^{sm}$  are approximately estimated as  $I_j^{sm/sp} \cdot \dot{\omega}_{wj}^{sm/sp} = C_{wj}^{sm/sp} - rT_{cj}^{sm/sp}$ . Additionally, the tangential contact forces have been reported for the first wheelset in Figure 10(b) and, to have a complete overview of the system dynamics, a comparison between the experimental and simulated sliding has been performed and reported in Figure 10(c).

In order to compare the old ‘global’ version of the adhesion model based on the Polach theory and developed by the authors in previous works (see the introduction and [32,33]) to the new ‘local’ one, in Table 5 the sliding and the adhesion coefficient estimation errors obtained by using the old ‘global’ model are reported as well. The match between simulated results and experimental data is good not only in terms of translational velocities but also in terms of sliding, rotational velocities and adhesion coefficients. The new ‘local’ model turns out to be slightly more accurate than the ‘local’ one but, at the same time, the new ‘local’ approach allows a more detailed description of the physical phenomena characterising degraded adhesion conditions.

Finally, to complete the analysis, the time histories of the simulated and the experimental torques  $C_{w1}^{sm}$ ,  $C_{w1}^{sp}$  applied to the first vehicle wheelset are reported in Figure 11.

In conclusion, the experimental validation of the adhesion model during the braking manoeuvre highlights the capability of the developed model in approximating the complex and highly non-linear behaviour of the degraded adhesion.

## 6. Simulation results

In this section, to better understand the behaviour of the contact pressures in the contact area, some simulated results are illustrated. For example, two simulation instants are considered (see Figure 9 and 10): the first one at 27s (high sliding and degraded adhesion

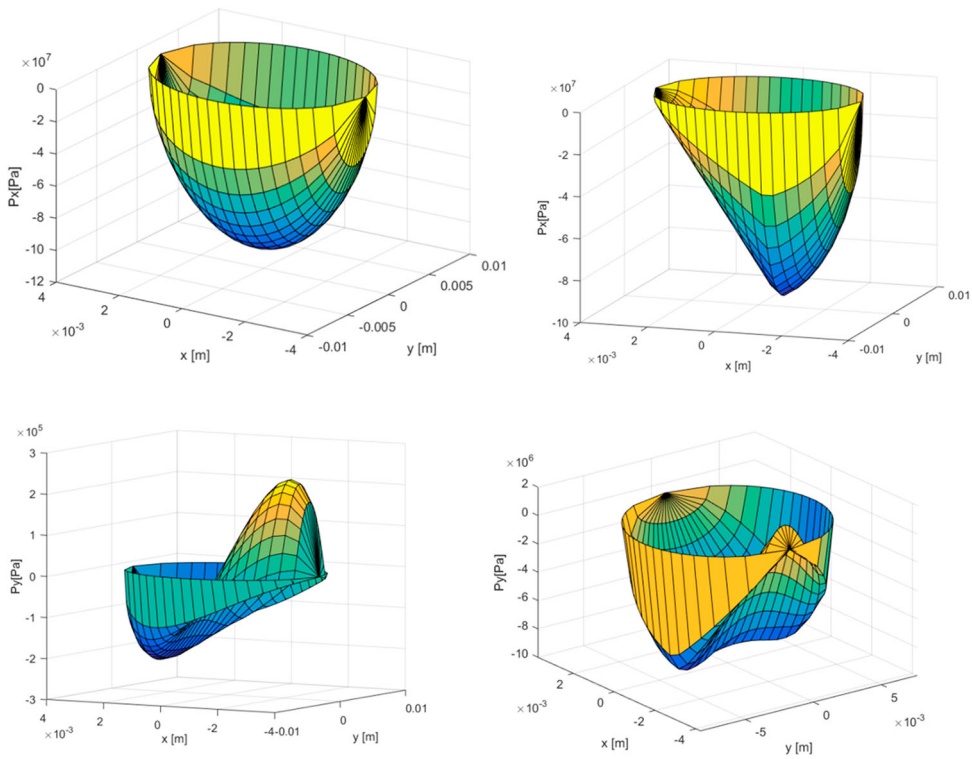


**Figure 12.** Tangential pressures  $p_{tx}$  and  $p_{ty}$  for the first wheelset (left wheel) in a pure sliding condition (up and down on the left) and in a partial adherence condition (up and down on the right).

conditions on the contact area) and the second one at 13s (lower sliding occurs and partial adherence on the contact area).

Longitudinal and lateral tangential contact pressures  $\underline{p}_t$  for the left wheel of the first wheelset at 27s, 13s are reported in Figure 12. Similarly, longitudinal and lateral local sliding  $\underline{s}$  for the left wheel of the first wheelset at 27s, 13s are illustrated in Figure 13. Figure 14 shows the dissipated energy  $W_{sp}$  in the contact area at 27s, 13s (left wheel of the first wheelset).

According to the tangential pressures  $\underline{p}_t$  and the sliding  $\underline{s}$ , only the slip area is present into the contact area at 27s when there is high sliding due to degraded adhesion. On contrary, both adhesion area and slip area occur at 13s when there are partial adherence conditions in the contact area. The dissipated energy  $W_{sp}$  behaves in agreement with  $\underline{p}_t$  and  $\underline{s}$ : naturally, the energy dissipation is higher under degraded adhesion conditions where higher sliding is present.

Concerning the onset of the adhesion recovery, looking at Figure 9 and Figures 12–14, it is interesting to observe that, during the braking, there are two time intervals characterised by high sliding: 14s – 17s and 23s – 31s (approximately). Naturally, during the first interval we have high sliding and energy dissipation but, being the interval quite short, the cleaning effect on the rail is not strong and long enough to trigger and maintain an adhesion recovery able to influence the global vehicle dynamics (for example the slope of the translation velocity curve is unchanged). On the contrary, being the second interval much longer than

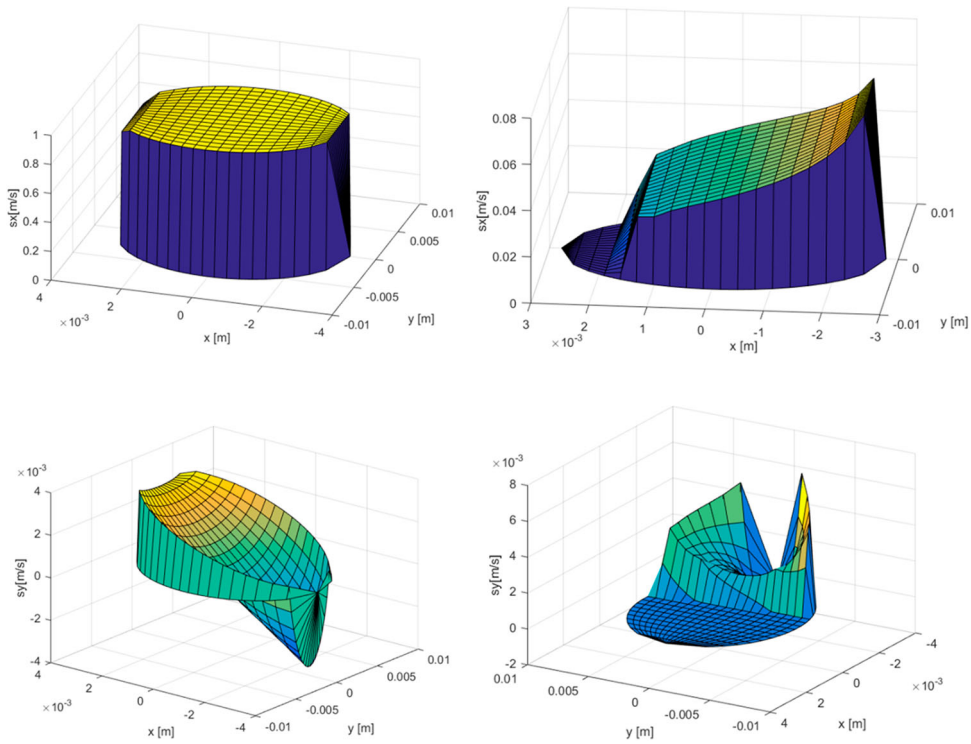


**Figure 13.** Local sliding  $s_x, s_y$  for the first wheelset (left wheel) in a pure sliding condition (up and down on the left) and in a partial adherence condition (up and down on the right).

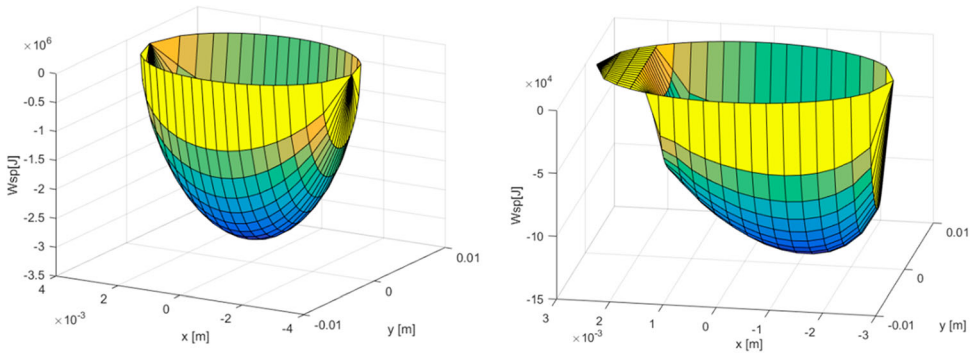


**Figure 14.** Dissipated energy  $W_{sp}$  for the first wheelset (left wheel) in a pure sliding condition (on the left) and in a partial adherence condition (on the right).

the first one, the high sliding and energy dissipation during this period lead to a cleaning effect that triggers an adhesion recovery long enough to deeply affect the global dynamics of the railway vehicles (see the important change of slope in the translation velocity curve during the second time interval).

In terms of numerical efficiency, the new model provided satisfying results. The computational load associated to the new adhesion model (Table 6 reports the mean

**Table 6.** Computational performances of the new degraded adhesion model.

Parameters	Unit	Value
Machine	(–)	HP Z620
CPU	(–)	Intel Xeon 2.60 GHz
RAM	(GB)	16
Mean time – new degraded adhesion model	(seconds to simulate 1s)	4.2
Mean time – FASTSIM	(seconds to simulate 1s)	2.5

computational times) is higher with respect the standard FASTSIM algorithm because the new model is clearly more complex. However, the efficiency of the new modelling strategy is still suitable for multibody applications (especially for large railway lines).

## 7. Conclusions

In this work the authors presented a new model to describe degraded adhesion conditions at the wheel–rail contact interface in railway vehicles. The new approach is suitable for multibody applications and characterised by satisfying computational performances, making possible implementation of the developed model inside complex vehicle multibody models. The new model is based on the main physical phenomena involved in the degraded adhesion such as the energy dissipation at the wheel–rail contact, the following cleaning effect and the final adhesion recovery caused by the destruction of the external contaminants. Since most of the physical characteristics of the contaminants are usually unknown and difficult to be measured, the new modelling strategy relies only on a few physical parameters (easy to be experimentally estimated).

The validation of the adhesion model is based on experimental data shared by Trenitalia S. p. A. and measured during some on-track tests performed in Velim (Czech Republic) with the railway vehicle UIC-Z1. The tests were carried out on a straight railway track under degraded adhesion conditions with a vehicle equipped with a Wheel Slide Protection (WSP) system.

Many important developments are scheduled for the future. Some theoretical improvements of the model will be considered, such as the modelling of third body layer and contaminants by means of the Reynolds equation. Furthermore, the proposed adhesion model will be more accurately validated not only through new on-field experimental campaigns but also using specific laboratory tests performed on dedicated test-rigs under more controlled conditions. This way a more deep and detailed validation of the new modelling strategy will be possible. Finally, some important topics like profile evolution due to wear and profile optimisation will be further investigated by using the new models developed in this work.

## Acknowledgements

The authors would like to thank Trenitalia S.p.A. for supplying the technical data and the experimental data related to the braking tests under degraded adhesion conditions and needed for the model validation.

## Disclosure statement

No potential conflict of interest was reported by the author(s).

## ORCID

Zhiyong Shi  <http://orcid.org/0000-0001-9985-8741>

## References

- [1] Polach O. Creep forces in simulations of traction vehicles running on adhesion limit. *Wear*. 2005;258:992–1000.
- [2] Auciello J, Meli E, Falomi S, et al. Dynamic simulation of railway vehicles: wheel/rail contact analysis. *Veh Syst Dyn*. 2009;47:867–899.
- [3] Falomi S, Malvezzi M, Meli E. Multibody modeling of railway vehicles: innovative algorithms for the detection of wheel–rail contact points. *Wear*. 2011;271(1–2):453–461.
- [4] Meli E, Falomi S, Malvezzi M, et al. Determination of wheel rail contact points with semi-analytic methods. *Multibody Syst Dyn*. 2008;20(4):327–358.
- [5] Shabana A, Tobaa M, Sugiyama H, et al. On the computer formulations of the wheel/rail contact problem. *Nonlinear Dyn*. 2005;40:169–193.
- [6] Shabana AA, Zaaza KE, Escalona JL, et al. Development of elastic force model for wheel/rail contact problems. *J. Sound Vib*. 2004;269:295–325.
- [7] Kalker J. Three-dimensional elastic bodies in rolling contact. Norwell: Kluwer Academic; 1990.
- [8] Antoine J, Visa C, Sauvey C, et al. Approximate analytical model for Hertzian elliptical contact problems. *J. Tribol*. 2006;128:660–664.
- [9] Ayasse J, Chollet H. Determination of the wheel–rail contact patch in semi-Hertzian conditions. *Veh Syst Dyn*. 2005;43:161–172.
- [10] Dukkipati R, Amyot J. Computer aided simulation in railway dynamics. New York (NY): Dekker; 1988.
- [11] Esveld C. Modern railway track. Delft: Delft University of Technology; 2001.
- [12] Johnson K. Contact mechanics. Cambridge: Cambridge University Press; 1985.
- [13] Kalker JJ. A fast algorithm for the simplified theory of rolling contact. *Veh Syst Dyn*. 1982;11:1–13.
- [14] Ignesti M, Malvezzi M, Marini L, et al. Development of a wear model for the prediction of wheel and rail profile evolution in railway systems. *Wear*. 2012;284–285:1–17.
- [15] Iwnicki S. Handbook of railway vehicle dynamics. London: Taylor and Francis; 2006.
- [16] Margheri S, Malvezzi M, Meli E, et al. An innovative wheel rail contact model for multibody applications. *Wear*. 2011;271(1):462–471.
- [17] Polach O. A fast wheel–rail forces calculation computer code. *Veh Syst Dyn*. 1999;33:728–739.
- [18] Pombo J, Silva A. A new wheel–rail contact model for railway dynamics. *Veh Syst Dyn*. 2007;45:165–189.
- [19] Voltr P, Lata M. Transient wheel–rail adhesion characteristics under the cleaning effect of sliding. *Veh Syst Dyn*. 2015;53(5):605–618.
- [20] Arias-Cuevas O, Li Z, Lewis R. A laboratory investigation on the influence of the particle size and slip during sanding on the adhesion and wear in the wheel–rail contact. *Wear*. 2011;271:14–24.
- [21] Arias-Cuevas O, Li Z, Lewis R, et al. Rolling–sliding laboratory tests of friction modifiers in dry and wet wheel–rail contacts. *Wear*. 2010;268:543–551.
- [22] Chen H, Ban T, Ishida M, et al. Experimental investigation of influential factors on adhesion between wheel and rail under wet conditions. *Wear*. 2008;265:1504–1511.
- [23] Descartes S, Desrayaud C, Niccolini E, et al. Presence and role of the third body in a wheel–rail contact. *Wear*. 2005;258:1081–1090.
- [24] Eadie D, Kalousek J, Chiddick K. The role of high positive friction (HPF) modifier in the control of short pitch corrugations and related phenomena. *Wear*. 2002;253:185–192.

- [25] Gallardo-Hernandez E, Lewis R. Twin disc assessment of wheel/rail adhesion. *Wear*. 2008;265:1309–1316.
- [26] Niccolini E, Berthier Y. Wheel–rail adhesion: laboratory study of ‘natural’ third body role on locomotives wheels and rails. *Wear*. 2005;258:1172–1178.
- [27] Wang W, Zhang H, Wang H, et al. Study on the adhesion behavior of wheel/rail under oil, water and sanding conditions. *Wear*. 2011;271:2693–2698.
- [28] Conti R, Meli M, Ridolfi E, et al. An innovative hardware in the loop architecture for the analysis of railway braking under degraded adhesion conditions through roller-rigs. *J Mechatron*. 2014;24(2):139–150.
- [29] Voltr P, Lata M, Cerny O. Measuring of wheel–rail adhesion characteristics at a test stand. XVIII International Conference on Engineering Mechanics; Svratka; 2012.
- [30] Zhang W, Chen J, Wu X, et al. Wheel/rail adhesion and analysis by using full scale roller rig. *Wear*. 2002;253:82–88.
- [31] Meli E, Ridolfi A. An innovative wheel–rail contact model for railway vehicles under degraded adhesion condition. *Multibody Syst Dyn*. 2015;33(3):285–313.
- [32] Allotta B, Meli E, Ridolfi A, et al. Development of an innovative wheel–rail contact model for the analysis of degraded adhesion in railway systems. *Tribol Int*. 2014;69:128–140.
- [33] Meli E, Pugi L, Ridolfi A. An innovative degraded adhesion model for multibody applications in the railway field. *Multibody Syst Dyn*. 2014;32(2):133–157.
- [34] Meli E, Ridolfi A, Rindi A. An innovative degraded adhesion model for railway vehicles: development and experimental validation. *Meccanica*. 2014;49:919–937.
- [35] Meacci M, Shi Z, Butini E, et al. A local degraded adhesion model for creep forces evaluation: an approximate approach to the tangential contact problem. *Wear*. 2019: 440–441.
- [36] Meacci M, Shi Z, Butini E, et al. A new local degraded adhesion model for railway applications including energy dissipation and adhesion recovery. 11th International Conference on Contact Mechanics and Wear of Rail/Wheel Systems; Delft; 2018.
- [37] TrenitaliaSpA. UIC-Z1 coach. Internal report of Trenitalia, Rome; 2000.
- [38] TrenitaliaSpA. WSP systems. Internal report of Trenitalia, Rome; 2006.
- [39] Malvezzi M, Meli E, Falomi S. Multibody modeling of railway vehicles: innovative algorithms for the detection of wheel-rail contact points. *Wear*. 2011;271(1):453–461.
- [40] Kelley C. Iterative methods for linear and nonlinear equations. Philadelphia (PA): SIAM; 1995.